Supporting Information

Surface-mediated Twin Polymerization of 2,2'-Spirobi[4*H*-1,3,2-benzodioxasiline] on Multi-walled Carbon Nanotubes, Polyacrylonitrile- and Copper Particles

Lysann Kaßner[a,b], Thomas Ebert[c], Patricia Godermajer[a], Volodymyr Dzhagan[d], Dietrich R. T. Zahn[e], Frank Simon[f], Doreen Dentel[g], Christoph Tegenkamp[g], Stefan Spange[c], and Michael Mehring[a,b,*]

a. Koordinationschemie, Technische Universität Chemnitz, 09107 Chemnitz, Germany. E-mail: michael.mehring@chemie.tu-chemnitz.de
b. Zentrum für Materialien, Architekturen und Integration von Nanomembranen (MAIN), Technische Universität Chemnitz Rosenbergstraße 6, 09126 Chemnitz, Germany.
c. Polymermaterialien, Technische Universität Chemnitz, 09107 Chemnitz, Germany
d. Lashkaryov Institute of Semiconductors Physics, NAS of Ukraine, 45 Nauky av., 03028 Kyiv, Ukraine
e. Halbleiterphysik, Technische Universität Chemnitz, 09107 Chemnitz, Germany. Zentrum für Materialien, Architekturen und Integration von Nanomembranen (MAIN), Rosenbergstraße 6, 09126 Chemnitz, Germany
f. Leibniz-Institut für Polymerforschung Dresden e.V., Hohe Straße 6, 01069 Dresden, Germany
g. Analytik an Festkörperoberflächen, Technische Universität Chemnitz, 09107 Chemnitz, Germany

The ESI part is organized according to substrate materials studied for surface modification corresponding to the order in the main text.

Content

1. Multi-walled carbon nanotubes (MWCNTs)

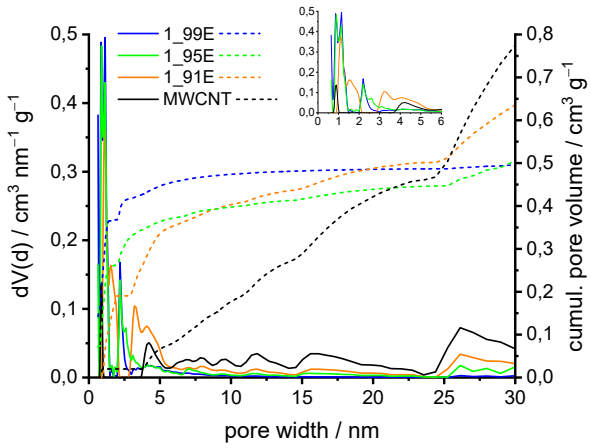

Figure S1. Pore size distributions (QSDFT model, equilibrium mode, slit and cylindrical pores) of the binary carbon//MWCNT composite materials obtained by polymerisation of 91 wt%, 95 wt, and 99 wt% TM on MWCNTs, thermal post-treatment and removal of silica with aqueous HF.

Table S1. Binary carbon//MWCNT composites produced by the thermal transformation of the phenolic resin-silica hybrid material-coated MWCNTs and subsequent etching by aqueous HF. Compositions were determined by quantitative elemental analyses and thermogravimetric measurements. Results of Raman spectroscopy show ratio of D and G absorption band and the position of the G-band.

sample	residue (TGA) [%]	carbon content [%]	I_D/I_G ratio	position G-band [cm^{-1}]
MWCNT	0.8	98.0	0.96	1585
1_91E	0	93.6	0.84	1588
1_95E	0	89.5	0.93	1588
1_99E	0	91.2	0.93	1591

The Raman spectrum of the MWCNTs shows, in contrast to graphite, a significant D-band which relates to literature data (Figure S1).[1,2] Compared to pristine MWCNTs, the Raman bands of carbon//MWCNT samples show a widening of the full width at half maximum. The position of the Raman bands is not significantly influenced as a function of composition.

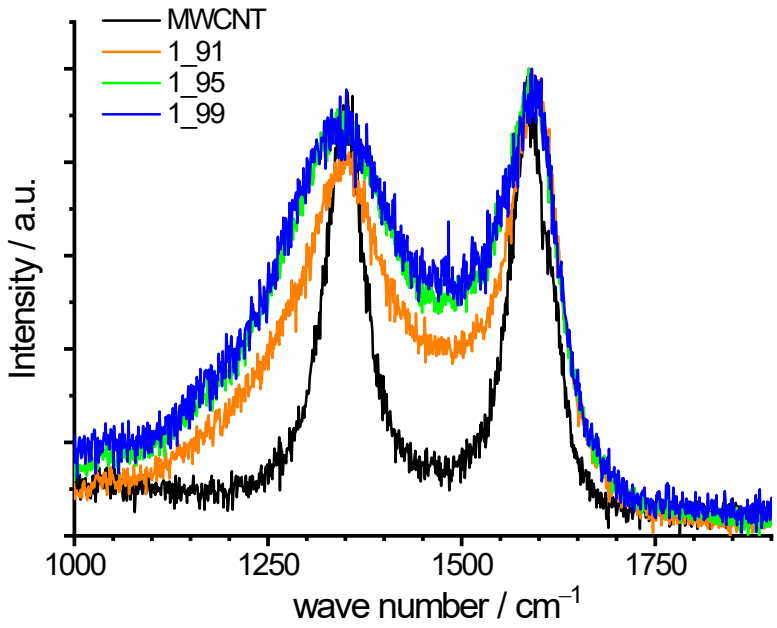

Figure S2. Normalized Raman spectra of carbon//MWCNT after etching with aqueous HF which vary in thickness of the amorphous carbon layer on MWCNT compared to the Raman spectrum of the starting MWCNT (laser wave length 514.7 nm).

2. PAN Powders

Experimental procedure for the thermal treatment of H-PAN:

H-PAN powder (5 g) was filled in a quartz glass tube with gas inlet. The tube was heated in a furnace under constant airflow and ambient pressure with a heating rate of 4 $K \cdot min^{-1}$ up to 250 °C. This temperature was held for two hours. Exhausting gas was directed through two gas-washing bottles connected in series (the first one containing an aqueous solution of $(NH_4)_2Fe(SO_4)_2$ and the other one an aqueous sodium hypochlorite (NaOCl) solution (pH = 13) to trap released HCN). This temperature was held for two hours. Afterwards the sample was slowly cooled to room temperature. A black powder in approximately 70 wt% yield was obtained. The elemental analyses (Table S2) are indicative for a reaction with oxygen due to an increasing content of the elements others than C, H and N. The as prepared thermally treated PAN (ttPAN) was used for further coating experiments.

Table S2. Elemental analyses of H-PAN, thermally treated PAN (ttPAN) and carbonised ttPAN (ttPAN_C).

sample	residue (TGA)	carbon content	hydrogen content	nitrogen content	remaining elements
	[%]	[%]	[%]	[%]	[%]
H-PAN	0.1	67.4	5.7	25.6	1.4
ttPAN	0	61.8	2.9	21.1	14.3
ttPAN_C	0	74.1	1.3	14.2	10.4

Thermal treatment lead to ring closure reactions resulting in aromatic structures as indicated by the $^{13}C\{^1H\}$ CP MAS NMR signals in the range from 130–160 ppm in solid state, which differ from those of as-received H-PAN powder from the manufacturer (Figure S2). Furthermore, the

intensity of CH and CH_2 NMR signals from the polymer backbone at 30 ppm decreases strongly. Carbonyl units at 170 ppm as well as C_{Aryl}–O units at 160 ppm are obtained for the thermally treated polymer as a sign for oxidative reactions with oxygen.[3–15]

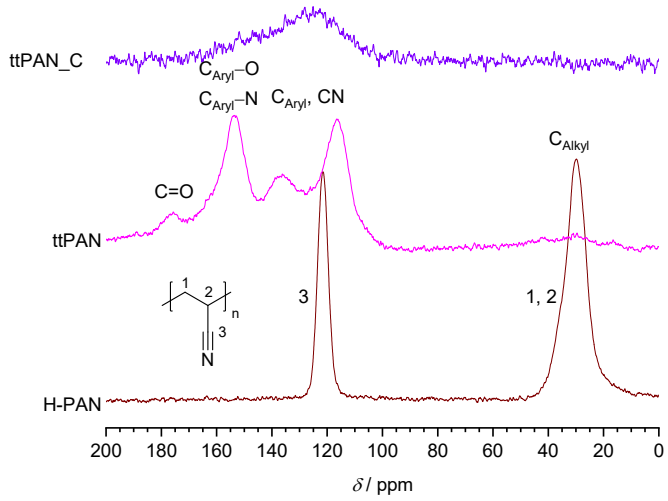

Figure S3. Solid State $^{13}C\{^1H\}$ CP MAS NMR spectra of PAN as-received (H-PAN) and after thermal treatment (ttPAN) in air and the after carbonisation (ttPAN_C).

The IR spectrum (Figure S3) of as-received PAN shows characteristic bands of C–H stretching vibration at 2940 cm^{-1} and C–H deformation at 1450 cm^{-1} from the polymer backbone as well as C≡N stretching vibration at 2243 cm^{-1}. After thermal treatment C=N and C=C stretching vibrations occur around 1560 cm^{-1} and out-of-plane-bending of C=C–H at 795 cm^{-1} (Figure S3).[9,12,14,15]

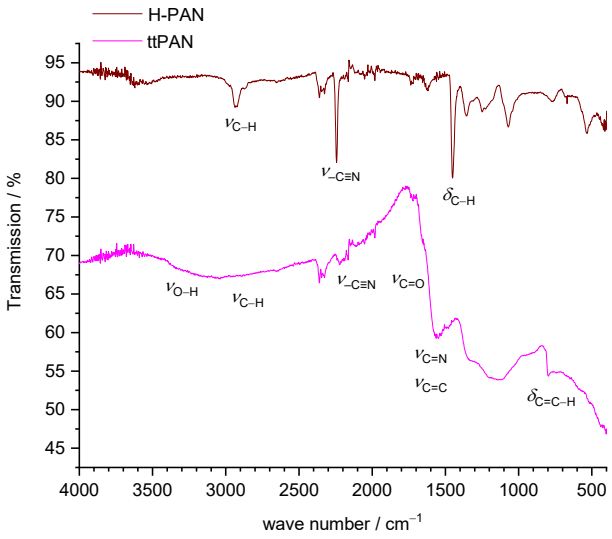

Figure S4. ATR-FTIR spectra of PAN (H-PAN) as-received and after thermal treatment (ttPAN) including characteristic vibrations.

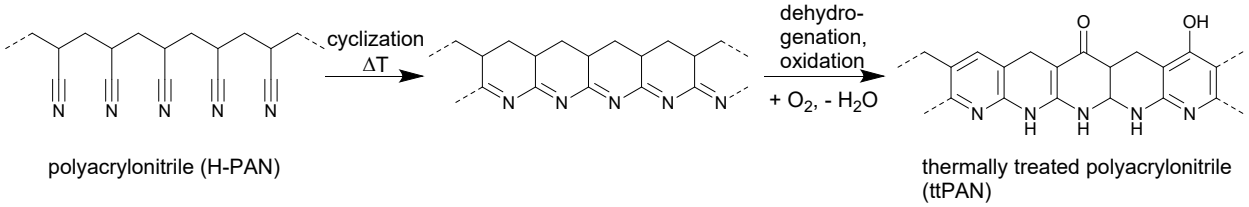

Scheme S1. Schematic illustration of structure formation during thermal treatment of H-PAN at 250 °C under airflow.[4,9,12]

For the determination of the appropriate polymerization reaction temperature of TM on ttPAN surface DSC measurements in melt were carried out for different mixtures (see Figure S4) of TM with ttPAN, DABCO, and H-PAN. H-PAN as well as ttPAN seem to hinder thermally induced twin polymerization of TM. Under the chosen conditions functional groups at the surface before and after thermal treatment do not catalyse the twin polymerization as can be considered from the onset temperatures for the polymerization process. With DABCO as base catalyst polymerization takes place.

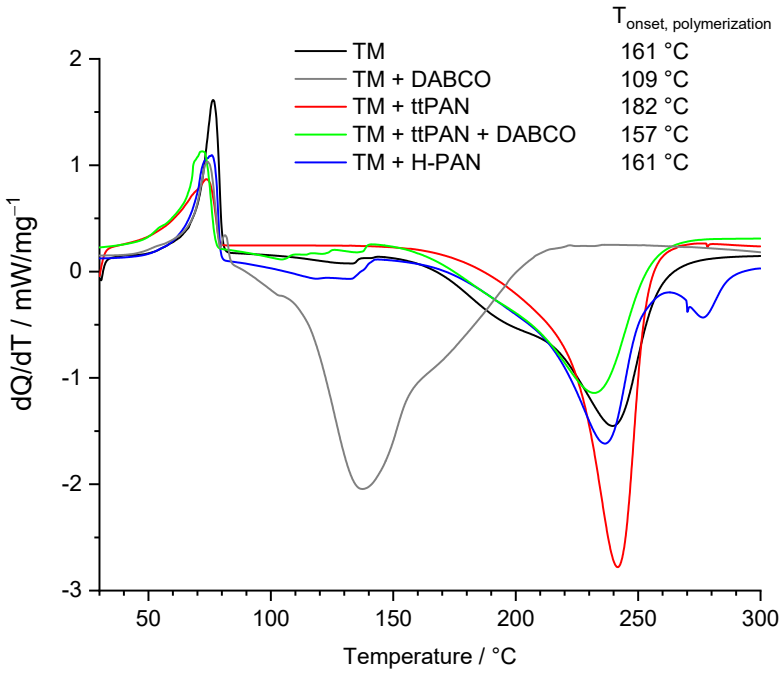

Figure S5. DSC graphs of TM and TM in the mixture with DABCO, H-PAN, and ttPAN, as well as ttPAN with DABCO as catalyst, with onset temperatures for the polymerization process, normalized on TM mass.

Therefore, as reference experiment under comparable conditions the TM was polymerized in DIPN with DABCO as catalyst at 160 °C for six hours resulting in a slightly turbid reaction mixture with completely dissolved, respectively, finely distributed hybrid material in DIPN. For this reason, separation by filtration as well as centrifugation was not successful. The hybrid material was precipitated by addition of *n*-hexane to the DIPN solution and filtered off to give 22 wt% yield. For all other coated ttPAN samples this flocculation procedure was not necessary and it was assumed that polymerization of TM occurred on the particle surface catalysed by adsorbed DABCO.

Table S3. Initial monomer contents and yields of phenolic resin-silica-coated ttPAN hybrid materials synthesized by DABCO-catalysed twin polymerization of 2,2'-spirobi[4*H*-1,3,2-benzodioxasiline] (TM) on ttPAN particles.

sample	initial monomer content [wt%]	yield total / TM [wt%]
ttPAN	0	-
2_25P	25	90 / 60
2_50P	50	77 / 55
2_70P	70	47 / 24
2_88P	88	61 / 56
TM_P	100	0 (22^{+}) / 0 (22^{+})

[+]yield after flocculation with *n*-hexane

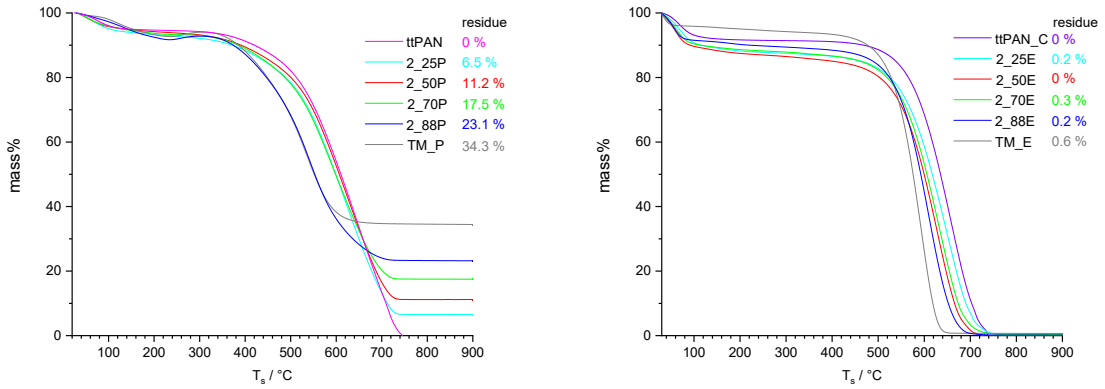

Figure S6. Thermogravimetric analyses under air of hybrid material-coated ttPAN particles compared to ttPAN (right) and carbonised hybrid material//*N*-doped carbon with subsequent etching by aqueous HF compared to ttPAN_C and carbonised and etched hybrid material of TM (left).

Solid state NMR experiments of the received hybrid material-coated ttPAN particles show the formation of phenolic resin in $^{13}C\{^{1}H\}$ CP-MAS NMR spectra (see Figure S5) as well as silica in $^{29}Si\{^{1}H\}$ CP-MAS NMR spectra (see Figure S6). Hence, for sample 2_88P remaining CH_2–O

units can be observed at 60 ppm due to incomplete polymerization or formation of etheric by-products.

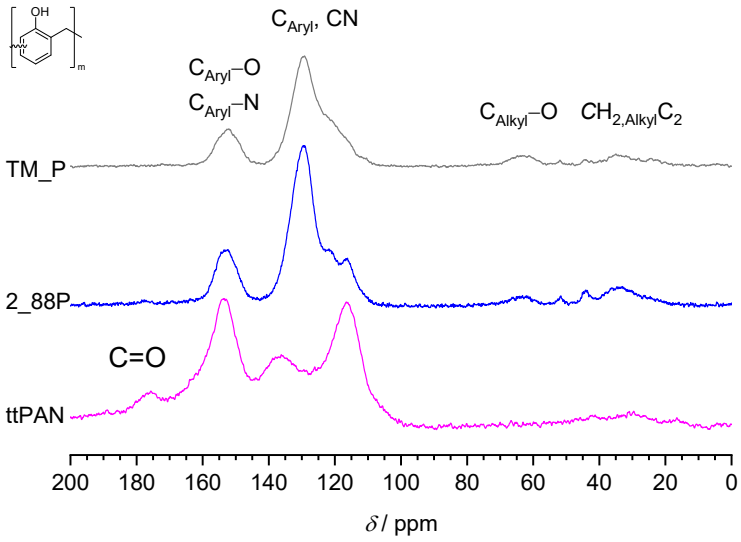

Figure S7. Solid state $^{13}C\{^1H\}$ CP MAS NMR spectra of polymerized twin monomer (TM_P) and coated ttPAN (2_88P) compared to thermally treated PAN (ttPAN).

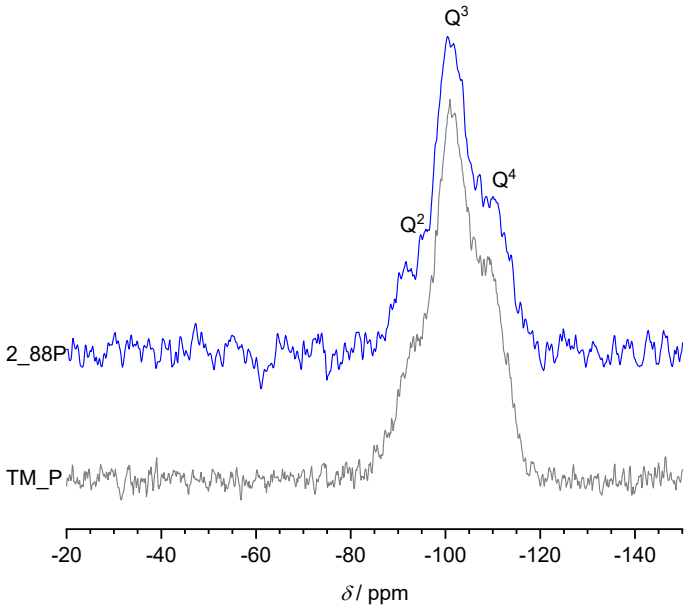

Figure S8. Solid state $^{29}Si\{^1H\}$ CP MAS NMR spectra of polymerized twin monomer TM (TM_P) and coated ttPAN (2_88P).

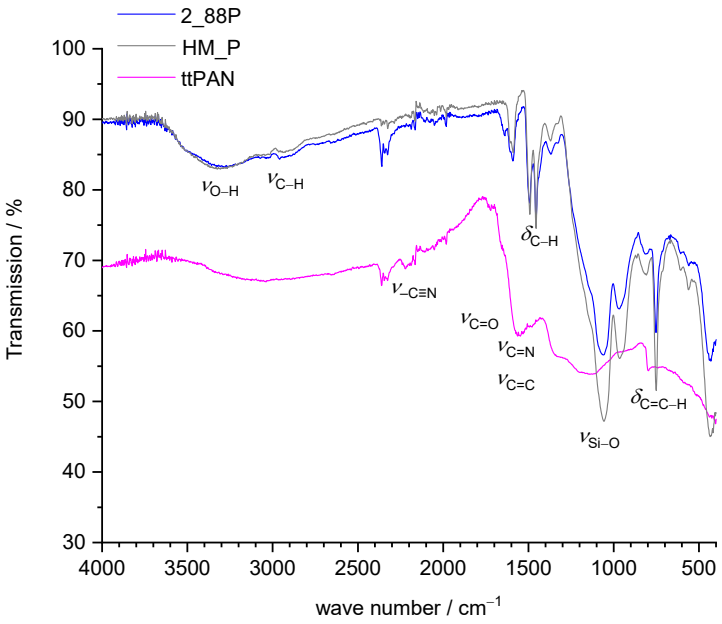

Figure S9. ATR-FTIR spectra of polymerized twin monomer (TM_P) and coated ttPAN (2_88P) compared to thermally treated PAN (ttPAN).

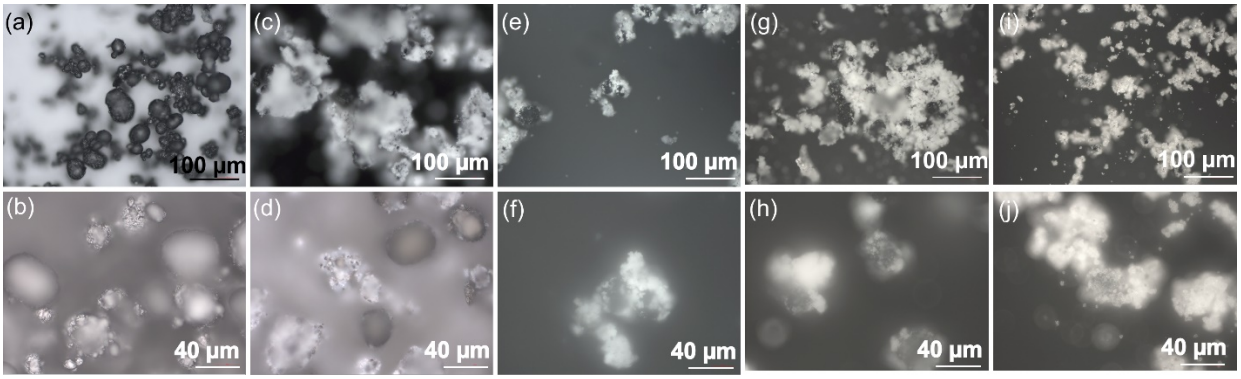

Figure S10. Light microscopy images in different magnifications of hybrid material-coated ttPAN particles 2_25P (c, d), 2_50P (e, f), 2_70P (g, h) and 2_88P (i, j) compared to ttPAN (a, b in darkfield modus).

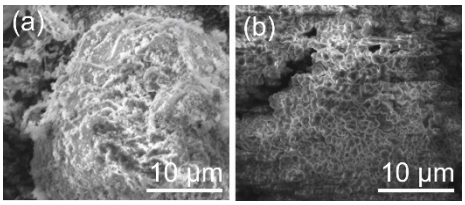

Figure S11. SEM micrographs of phenolic resin-silica hybrid material-coated ttPAN particles obtained by DABCO-catalyzed surface twin polymerization using 25 wt% (a), and 88 wt% (b) of TM 10,000x magnification.

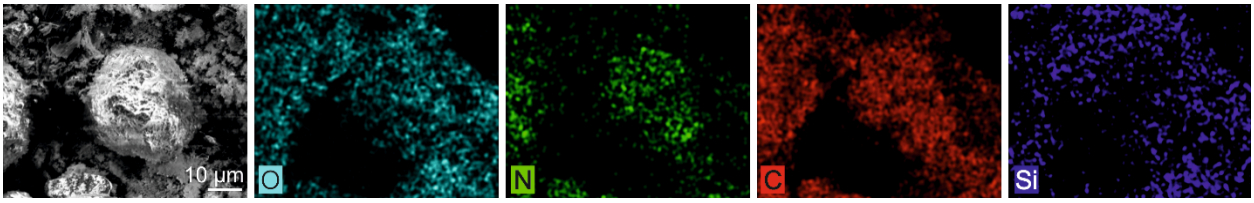

Figure S12. SEM of functionalized ttPAN particles 2_25 with EDX measurement with elemental distribution of C, N, Si and O.

Table S4. Binary carbon//*N*-carbon composite 2_95E produced by the thermal transformation of the phenolic resin-silica hybrid material-coated PAN particles 2_95P (n_{TM} : n_{DABCO} = 50 : 1) after etching with HF compared to etching with aqueous NaOH (5 M, 3 hours reflux).

Sample	surface area [m^2 g^{-1}]		overall pore volume	microporous volume	microporous fraction
	BET	QSDFT	[cm^3 g^{-1}]	[cm^3 g^{-1}]	[%]
2_95E_HF	1488	1267	0.7161	0.3511	49.0
2_95E_NaOH	1153	886	0.5783	0.2582	44.6

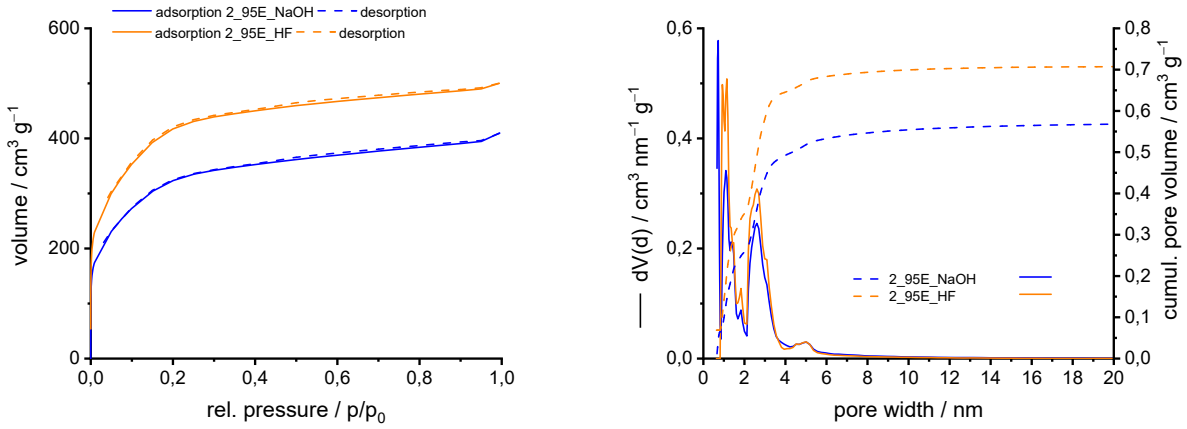

Figure S13. Nitrogen sorption isotherms (left) and pore size distributions (right) of the binary carbon//*N*-carbon composite materials 2_95E_HF and 2_95E_NaOH achieved by twin polymerization of TM on ttPAN, thermal transformation into carbon-silica//*N*-carbon and removal of silica by HF compared to removal by aqueous NaOH.

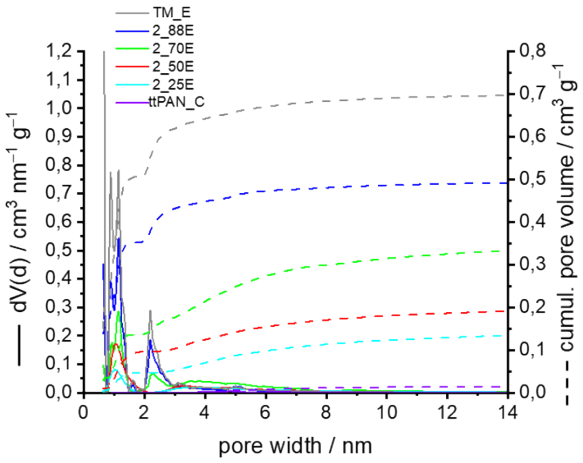

Figure S14. Pore size distributions (QSDFT model, equilibrium mode, slit and cylindrical pores) of the binary carbon//*N*-carbon composite materials obtained by polymerisation of TM and 25 wt%, 50 wt, 70 wt%, and 88 wt% TM on PAN, thermal post-treatment under argon and removal of silica with aqueous HF compared to ttPAN after pyrolysis under argon (ttPAN_C)

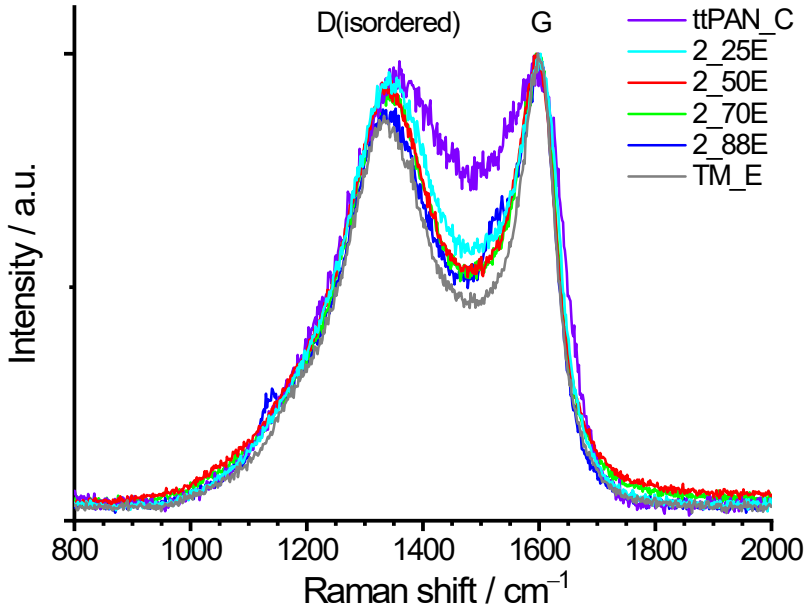

Figure S15. Normalized Raman spectra of carbon//*N*-carbon after etching which vary in thickness of the amorphous carbon layer on carbonised ttPAN compared to the Raman spectrum of the carbonised ttPAN (laser wave length 532 nm).

All samples exhibit D and G bands at around 1340 cm^{-1} and 1600 cm^{-1}, respectively, indicating that ttPAN is partly in graphitic form (Figure S13 and Table S5).[10] G band shows ordered graphitic crystallites whereas the D bands relates to disordered structures. Bands of pristine carbonised ttPAN show a larger width at half maximum, compared to coated and carbonised ttPAN particles. The band position is not significantly influenced as a function of composition. That hints to clusters of different orders and dimensions in amorphous carbon from carbonised ttPAN.[1] I_D/I_G ratio is between 0.89 and 0.98. The lower this value is the higher are crystallinity and electrical conductivity.[10]

Table S5. Binary carbon//*N*-carbon composites after etching with HF produced by the thermal transformation of the phenolic resin-silica hybrid material-coated PAN particles. Compositions were determined by quantitative elemental analyses and thermogravimetric measurements. Results of Raman spectroscopy show ratio of D and G absorption band and the position of the G-band.

Sample	Residue (TGA) [%]	Carbon content [%]	Nitrogen content [%]	I_D/I_G ratio	Position G-band [cm^{-1}]
ttPAN_C	0	73.0	14.1	0.98	1598
2_25E	0.2	71.7	12.0	0.96	1603
2_50E	0	72.0	11.3	0.94	1596
2_70E	0.3	72.1	12.9	0.93	1595
2_88E	0.2	79.3	4.8	0.91	1599
TM_E	0.6	86.8	0	0.89	1598

3. Copper Powder

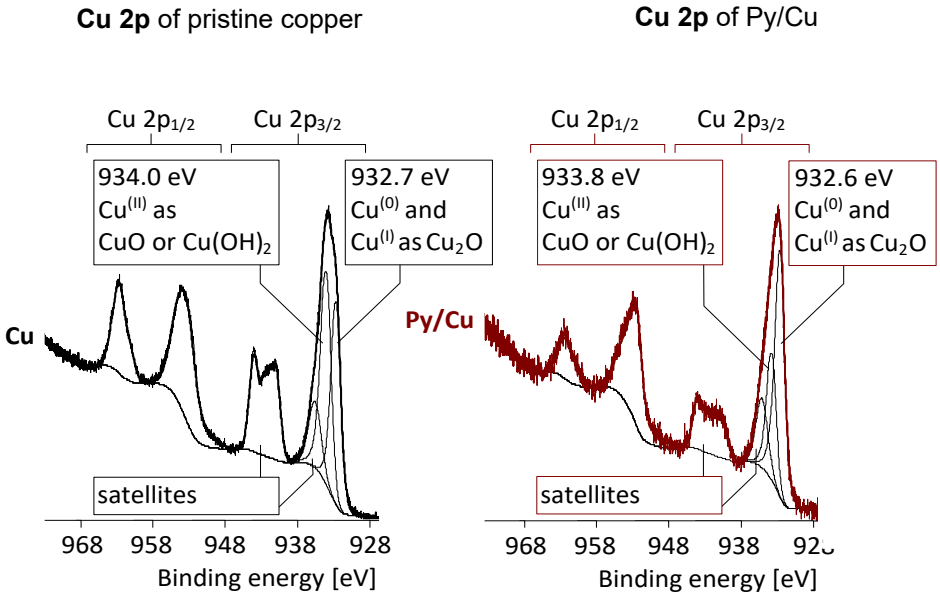

Figure S16. Cu 2p XP spectra recorded from pyrrolidine-modified copper particles (**Py/Cu**) compared to the XP spectra recoded from the pristine copper sample (**Cu**).[16,17]

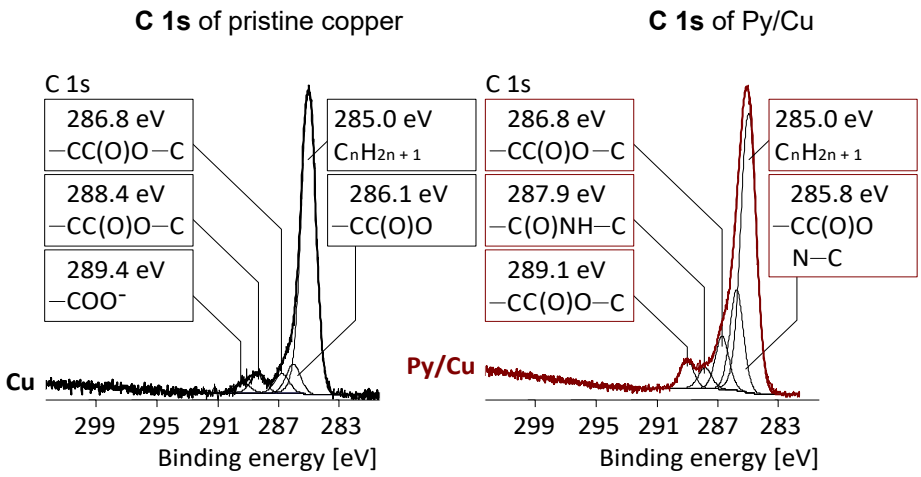

Figure S17. C 1s XP spectra recorded from pyrrolidine-modified copper particles (**Py/Cu**) compared to the XP spectra recoded from the pristine copper sample (**Cu**).

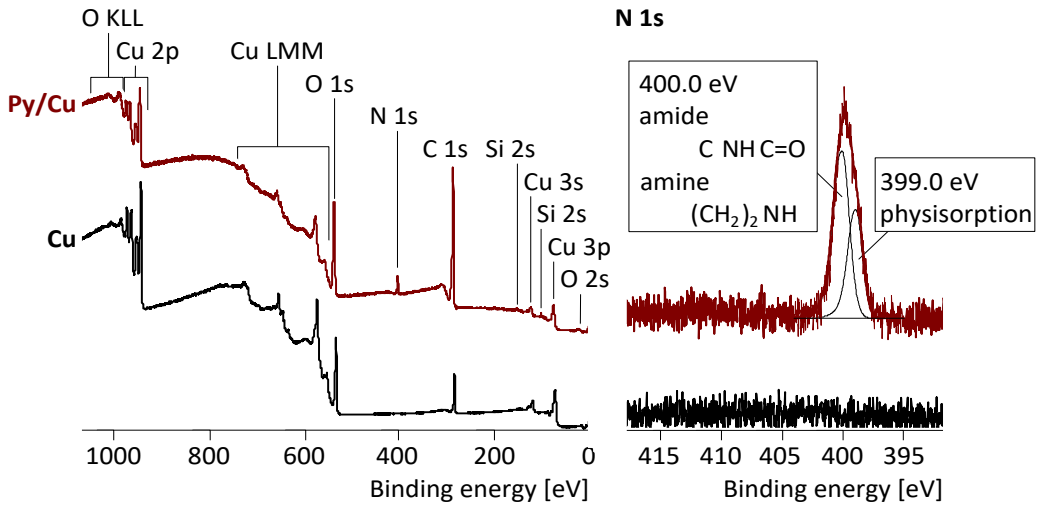

Figure S18. Wide-scan (left) and N 1s (right) XP spectra recorded from pyrrolidine-modified copper particles (**Py/Cu**) compared to the XP spectra recoded from the pristine copper sample (**Cu**).[16,18–22]

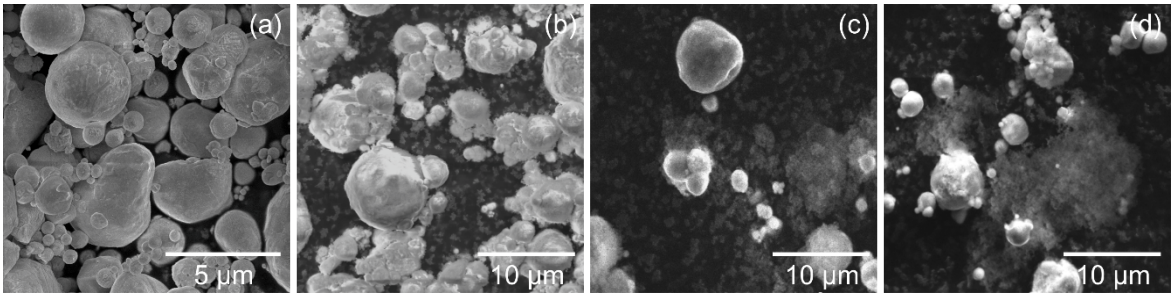

Figure S19. SEM of bare copper (a) and functionalized copper particles 3_33 (b), 3_20 (c), and 3_10 (d).

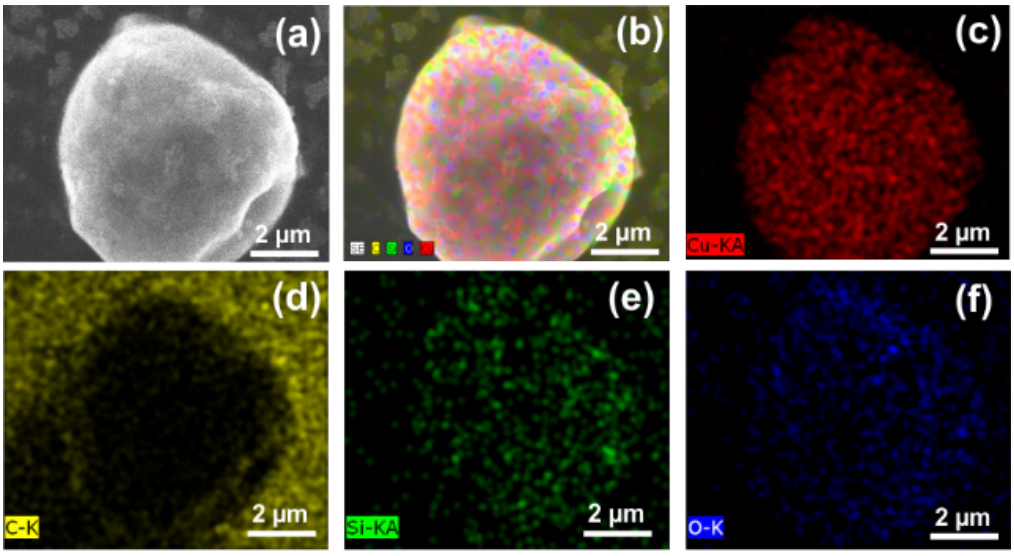

Figure S20. SEM of functionalized copper particles 3_20 with EDX measurement with elemental distribution of C, Cu, Si, and O

Literature

1 A. C. Ferrari and J. Robertson, *Phys. Rev. B*, 2000, **61**, 14095–14107.
2 A. Jorio, M. A. Pimenta, A. G. S. Filho, R. Saito, G. Dresselhaus and M. S. Dresselhaus, *New J. Phys.*, 2003, **5**, 139–139.
3 S. K. Nataraj, K. S. Yang and T. M. Aminabhavi, *Prog. Polym. Sci.*, 2012, **37**, 487–513.
4 E. Fitzer, W. Frohs and M. Heine, *Carbon*, 1986, **24**, 387–395.
5 D. Braun and R. Disselhoff, *Angew. Makromol. Chem.*, 1978, **74**, 225–248.
6 S. Lee, J. Kim, B.-C. Ku, J. Kim and H.-I. Joh, *Adv. Chem. Eng. Sci.*, 2012, **02**, 275–282.
7 R. F. Ribeiro, L. C. Pardini, N. P. Alves and C. A. R. Brito Júnior, *Polímeros*, 2015, **25**, 523–530.
8 O. A. Belyaeva, D. I. Krivtsov, A. V. Gaberling and V. Ya. Varshavskii, *Fibre Chem.*, 2013, **44**, 268–272.
9 S. Dalton, F. Heatley and P. M. Budd, *Polymer*, 1999, **40**, 5531–5543.
10 İ. Gergin, E. Ismar and A. S. Sarac, *Beilstein J. Nanotechnol.*, 2017, **8**, 1616–1628.
11 M.-C. Yang and D.-G. Yu, *Text. Res. J.*, 1996, **66**, 115–121.
12 M. S. A. Rahaman, A. F. Ismail and A. Mustafa, *Polym. Degrad. Stab.*, 2007, **92**, 1421–1432.
13 J.-H. Yun, B.-H. Kim, K.-S. Yang, Y.-H. Bang, S.-R. Kim and H.-G. Woo, *Bull. Korean Chem. Soc.*, 2009, **30**, 2253–2258.
14 E. Cipriani, M. Zanetti, P. Bracco, V. Brunella, M. P. Luda and L. Costa, *Polym. Degrad. Stab.*, 2016, **123**, 178–188.
15 Z. Fu, Y. Gui, S. Liu, Z. Wang, B. Liu, C. Cao and H. Zhang, *J. Appl. Polym. Sci.*, , DOI:10.1002/app.40834.
16 J. F. Moulder, W. F. Stickle, P. E. Sobol, K. D. Bomben, J. Chastain, R. C. King Jr. and Physical Electronics, Incorporation, Eds., *Handbook of X-ray photoelectron spectroscopy: a reference book of standard spectra for identification and interpretation of XPS data*, Physical Electronics, Eden Prairie, Minn., 1995.
17 I. Gallardo, J. Pinson and N. Vilà, *J. Phys. Chem. B*, 2006, **110**, 19521–19529.
18 X.-L. Chen, L.-S. Ma, W.-Y. Su, L.-F. Ding, H.-B. Zhu and H. Yang, *Electrochimica Acta*, 2020, **331**, 135273.
19 W. Jin, Z. Lu, Q. Wang, Y. Zhu, H. Pan, S. Yao, Z. Fang, X. Huang and X. Chen, *J. Phys. Mater.*, 2021, **4**, 024006.
20 M. Šetka, R. Calavia, L. Vojkůvka, E. Llobet, J. Drbohlavová and S. Vallejos, *Sci. Rep.*, 2019, **9**, 8465.
21 X. Xie, J. Liu, T. Li, Y. Song and F. Wang, *Chem. – Eur. J.*, 2018, **24**, 9968–9975.
22 C. Huang, L. Zheng, W. Feng, A. Guo, X. Gao, Z. Long and X. Qiu, *ACS Sustain. Chem. Eng.*, 2020, **8**, 14030–14038.